UNIVERSITI PUTRA MALAYSIA

EFFECT OF GROWTH TIME ON STRUCTURAL, ELECTRICAL AND MORPHOLOGICAL PROPERTIES OF MANGANESE DIOXIDE NANOWIRES

IZZUDDIN BIN MOHD ZAHARUDDIN

EFFECT OF GROWTH TIME ON STRUCTURAL, ELECTRICAL AND MORPHOLOGICAL PROPERTIES OF MANGANESE DIOXIDE NANOWIRES

By

IZZUDDIN BIN MOHD ZAHARUDDIN

Thesis Submitted to the Department of Physics, Universiti Putra Malaysia, in partial Fulfilment of the Requirements for the Degree of Bachelor of Science in Physics with Honours

February 2022

DEDICATION

This study I particularly dedicate to Dr Tan Sin Tee, my supervisor of my final year project, my parents, my mentor and my friends who are patiently guiding me one by one, gave me strength when I thought to give up and continually provide their support and time during this thesis completion.

ABSTRACT

EFFECT OF GROWTH TIME ON STRUCTURAL, ELECTRICAL AND MORPHOLOGICAL PROPERTIES OF MnO_2 NANOWIRES

By

Izzuddin bin Mohd Zaharuddin

199026

February 2022

Supervisor: Dr. Tan Sin Tee

Faculty: Faculty of Science

Phase transformation and surface modification of Metal-Transition Oxide (TMO) Materials had emerged an interest study due to its excellent anisotropy property in optoelectronic devices. There is various approach has been implemented to modify the nanostructure which is not limited to the doping, physic controlled growth and surfactant controlled system. Among the TMO materials, MnO_2 is recognized as one of the outstanding materials that is commonly used in the green energy storage devices, owing to its polymorphic nature. However, the detail understanding in the phase transformation mechanism and properties modification of this material is remain uncertain. In this project, a detail correlation between the structural changes of MnO_2 nanowires was study in term of different growth time. The kinetic and thermodynamic growth system in the phase changes was also elucidate. When the growth time increased from 3h to 9h, the MnO_2 nanowire was found successfully transformed from hollandite phase α-MnO_2 to pyrolusite

® phase (β-MnO_2) before further extend to λ-MnO_2. This result is further validated from the decreasing of crystalline size as calculated from the XRD analysis. Furthermore, the changes of the tunnel structures in MnO_2 nanowires also leading to the highest conductivity as recorded in the 3h MnO_2 sample. This result had proved that the different growth time has resulting to the phase and structural transformation in MnO_2 nanowire design. This approach can be used as a benchmark methodology for fundamental understanding in polymorphous formation that applicable in optoelectronic devices.

ABSTRAK

KESAN MASA PERTUMBUHAN PADA SIFAT STRUKTUR, ELEKTRIKAL DAN MORFOLOGI MnO_2 NANOWAYAR

Oleh

Izzuddin bin Mohd Zaharuddin

199026

Februari 2022

Penyelia: Dr. Tan Sin Tee

Fakulti: Fakulti Sains

Transformasi fasa dan pengubahsuaian permukaan bahan Oksida Logam Peralihan (TMO) telah muncul sebagai kajian yang mendapat perhatian yang tinggi kerana sifat anisotropinya yang sangat baik dalam peranti optoelektronik. Terdapat pelbagai pendekatan telah dilaksanakan untuk mengubah suai struktur nano yang tidak terhad kepada kaedah pendopan, sistem pertumbuhan terkawal dan ketegangan permukaan terkawal. Di antara bahan TMO, MnO_2 diiktiraf sebagai salah satu bahan terunggul yang biasa digunakan dalam peranti penyimpan tenaga hijau, kerana sifat polimorfiknya. Walau bagaimanapun, pemahaman terperinci dalam mekanisme transformasi fasa dan pengubahsuaian sifat bahan ini masih kekal tidak jelas. Dalam projek ini, perubahan dan sifat struktur wayar nano MnO_2 telah dikaji menggunakan masa pertumbuhan yang berbeza. Sistem pertumbuhan kinetik dan termodinamik dalam perubahan fasa juga dijelaskan. Apabila masa pertumbuhan meningkat daripada 3j kepada 9j, wayar nano

MnO_2 didapati berjaya diubah daripada fasa hollandite (α-MnO_2) kepada fasa pirolusit (β-MnO_2) sebelum melanjutkan lagi ke fasa λ-MnO_2. Keputusan ini selanjutnya disahkan lagi dengan pengurangan saiz kristal seperti yang dikira daripada analisis XRD. Tambahan pula, perubahan struktur terowong dalam wayar nano MnO_2 juga membawa kepada kekonduksian tertinggi seperti yang direkodkan dalam sampel MnO_2 3h. Keputusan ini telah membuktikan bahawa masa pertumbuhan yang berbeza telah menyebabkan fasa dan transformasi struktur dalam reka bentuk wayar nano MnO_2. Pendekatan ini boleh digunakan sebagai metodologi penanda aras untuk pemahaman asas dalam pembentukan polimorf yang boleh digunakan dalam peranti optoelektronik.

ACKNOWLEDGMENT

I would like to take this opportunity to express my gratitude to everyone that contributed a great amount of assistance to me until I successfully complete this thesis.

First and foremost, I would like to express my deepest appreciation to my supervisor, Dr Tan Sin Tee who is patiently provide guidance, support and motivation to me throughout the duration of this project although she in the postpartum period. Her dedication, insightful suggestion as well as her profound belief in my abilities have helped me in a lot of ways upon completing our final project. Thank you, Dr.,

I am also thankful to the Ministry of Higher Education of Malaysia for its financial assistance under the study grant FRGS/1/2019/STG07/UPM/02/5.

Next, I would like to extend my sincere thanks to Universiti Putra Malaysia that provided the facilities, well-equipped apparatus and equipment to be utilised in this work. Special thanks to all Advanced Material Device Laboratory (AMDL) members, Jun Yan Lim, Kai Jeat Hong and others for providing technical assistance in preparing and characterizing the samples.

Other than that, I am also grateful to my friends and coursemates who were always supporting me in the journey of completing this work. I would like to thank them that kindly shared any information or knowledge with me.

Finally, I wish to extend my gratitude to my family that provide unrelenting support and great love towards me. This project would not be possible without their unwavering support.

TABLE OF CONTENTS

LIST OF FIGURES

LIST OF TABLES

LIST OF ABBREVIATIONS

FESEM	Field-emission scanning electron microscopy
FWHM	Full width at half maximum
MDO	Metal dioxide
MnO_2	Manganese dioxide
MnO_2-3H	3 hours growth time MnO_2 sample
MnO_2-5H	5 hours growth time MnO_2 sample
MnO_2-7H	7 hours growth time MnO_2 sample
MnO_2-9H	9 hours growth time MnO_2 sample
RS	Raman scattering
TMO	Transitional-metal oxide
TEM	Transmission electron microscopy
XRD	X-ray diffraction
4PP	Four-point probe

CHAPTER 1

INTRODUCTION

1.1 Research Background

An intense Research and Development focus on nanotechnology has been delivered in recent years, particular in renewable energy. These nanomaterials have undergone extensive study in order to develop a new technique that used in energy storage technology. Among various substances and materials, transitional metal oxides like NiO, Co_3O_4, SnO_2 have been extensively studied as supercapacitor materials. Among them, MnO_2 receive much attention due to its large theoretical specific areas, wide potential window, the abundant amount in nature and environment friendly.

Mineral manganese dioxide with black pigments properties has been used for rock-art painting in palaeolithic caves. Today, MnO_2 is an important material, which is technologically attractive for application in different fields like catalysts, absorbent of toxic metals, ion sieves, molecular sieves, artificial oxidase, component of the dry cell, an inorganic pigment in ceramics, electrodes for electrochemical batteries and electrode for supercapacitors (Julien & Mauger, 2017). Nanostructured manganese dioxides (MnO_2) are among the excellent materials for high-performance electrochemical energy storage devices, including batteries and supercapacitors that have been in high demand for use in this electronics era.

The great interest of MnO_2 as an inorganic material in the battery industry is due to its high theoretical capacity and capacitance, natural abundance, low cost and toxicity. MnO_2 exists in various crystallographic phase including α-, β-, γ-, and δ, which are naturally polymorph compound. The polymorphism is due to the different ways of linking the MnO_6 octahedra units through the corner or edge-sharing that produce variations in the chain and tunnel structure. There are three common types of MnO_2 crystal phase which can be classified from their tunnel dimension (m x n) such as hollandite with (2 x 2), pyrolusite with (1 x 1) and birnessite with (1 x ∞). The structural, morphological and electrical properties of MnO_2 are easily modified via various synthesis approaches by altering theirs crystalline structure, particle size, and morphology.

1.2 Problem Statement

A great attention has been paid to the synthesis aspect of the MnO_2 because most of their performance strongly depends on the preparation process that also determines the morphology, type and size of the nanostructure. Polymorphs of MnO_2 significantly depend on the synthesis conditions such as reactant concentration, growth time, precursor, temperature, etc. Several routes are currently used to synthesis nanostructured MnO_2 samples with different controlled morphologies (shape and size). The synthetic methods for nanostructured MnO_2 include simple reduction, coprecipitation, sol-gel, thermal decomposition, and the hydrothermal synthesis molten-salt method (R. Liu et al., 2013). Various nanostructured objects investigated over the years include nanowires, nanorods, nanoflowers, nanosheets, etc.

Wang et al. (2002) synthesised β-MnO_2 hydrothermally by a reaction between $MnSO_4$ and $(NH_4)_2S_2O_8$ and obtained α-MnO_2 after the addition of $(NH_4)_2SO_4$. In other studies, Li et al. (2005) prepared α-MnO_2 at room temperature, obtaining β-MnO_2 hydrothermally at 80 ◦C. In addition, Subramanian et al. (2005) studied a hydrothermal formation process of α-MnO_2 at 140 ◦C from 1 to 18 h and observed the development of nanowires from flower-like MnO_2 particles obtained by the reaction between $MnSO_4$ and $KMnO_4$.

In addition, there are a method to obtaining one polymorph from another; for example, Wei et al. (2005) successfully transformed γ -MnO_2 into α- and β-MnO_2 at 140 and 170 ◦C, respectively. Ferreira et al. (2006) use hydrothermal transformation in a dodecyl amine aqueous solution, from δ-MnO_2 into MnOOH, which can be subsequently tempered at 300–500 ◦C to form β-MnO_2. In addition, Shen et al. (2005) reported a transformation from δ-MnO_2 into other polymorphs of MnO_2 with (2 × 4), (2 × 3) and (1 × 1) tunnel structure at pH = 13, 7 and 1, respectively. We believe the pH value will affect the formation of polymorphs significantly.

Although great efforts and attention have been made to controlling the crystal type, size and morphology of MnO_2, **a complete understanding of MnO_2 growth and transformation mechanism is remain unclear in current literature.** Additionally, the **slow crystal growth rate in MnO_2 nanostructure** also need to be studied to create an optimum system for MnO_2 crystal growth mechanism.

1.3 Research Objectives

The objectives of this study are as follows:

- To synthesis MnO_2 nanowires using hydrothermal method.
- To investigate the effect of growth time on structural, electrical and morphological properties of MnO_2 nanowires
- To explain the crystal growth mechanism of MnO_2 nanowire in the function of growth time

CHAPTER 2

LITERATURE REVIEW

2.1 Introduction

Manganese dioxide (MnO_2) has many important applications, such as ionic and molecular sieves, catalysts, and cathode materials for rechargeable batteries. MnO_2 shows a huge structural flexibility and appears in a number of crystallographic polymorphs, such as α-, β-, γ -, δ-and ε-MnO_2 (Gao et al., 2009). This chapter discusses recent information in MnO_2 crystal study, synthetic methods and conditions, and MnO_2 growth mechanism.

2.2 Manganese Dioxide, MnO_2

MnO_2 structures can be described as a close-packed network of oxygen atoms in which Mn^{4+} cations (ionic radius of 0.53 Å) are differently distributed. These distributions are conveniently described by filled [MnO_6] octahedra sharing opposite octahedral edges to form endless chains, which can in turn be linked to neighbouring octahedral chains by sharing corners or edges. The manganese dioxides can be classified according to the number of MnO_6 units and the number of MnO_6 octahedral chains between two basal layers to form tunnel (m x n) openings (Julien et al., 2017).

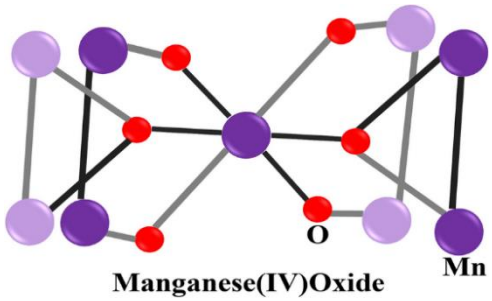

Figure 2.1 Ball-and-stick model of MnO2 unit cell (oxygen atoms are coloured red, manganese atoms are violet)

MnO_2 crystallographic forms including the α-, β-, γ-, δ- ε-, λ- and R-polymorphs, which are naturally occurring minerals such as hollandite (2 × 2), pyrolusite (1 × 1), nsutite (1 × 1)/(1 × 2) with hexagonal (hex.) structure, birnessite (1 × ∞), akhtenkite (dense stack), spinel (1 × 1), and ramsdellite (1 × 2), respectively, where (m × n) denotes the tunnel dimension, making MnO_2 polymorphs ideal for application in ion transport and storage, such as rechargeable ion batteries. For larger tunnels such as the (2 x 2) tunnels and (3 x 3) tunnels, the large opening typically requires the presence of hydrated cations within the tunnel to prevent structural collapse such as K^+, Ba^{2+} and Pb^+.

β-MnO_2 or pyrolusite forms in the rutile structure with MnO_6 octahedra connecting along edges to form chains. These chains connect via corner sharing to form a tunnelled structure, Figure 2.2a. The tunnels align along a direction and have the dimension of a one-by-one octahedron (1 x 1). β-MnO_2 is the thermodynamically stable MnO_2 polymorph at ambient conditions. In α-MnO_2, two chains connect via edge sharing, and the double chains then connect through corner-sharing to form two by two (2x2) and (1x1) tunnels extending along a direction, Figure 2.2c. The larger (2x2) tunnels are stabilised by large ions such as K^+, Ba^{2+} and Pb^+. Therefore, α-MnO_2 has the chemical formula K_xMnO_2 (x

≈ 0.16) and the average oxidation state of the manganese ion is less than four. For δ-MnO_2, the MnO_6 octahedra connect via edges in two dimensions forming MnO_2 sheets. The sheets stack in parallel forming a layered structure, Figure 2.2d. The structure is relatively open and different ions and molecules can reside in between the MnO_2 sheets. The nature of the stacking and the distance between the MnO_2 layers can vary, giving phases of different symmetry (space group). Despite of this, many MnO_2 phases have the same overall structural pattern of stacked MnO_2 sheets, and they are all referred to as δ-MnO_2. (Julien et al., 2017). The crystallographic data of some MDO compounds are summarised in Table 2.1.

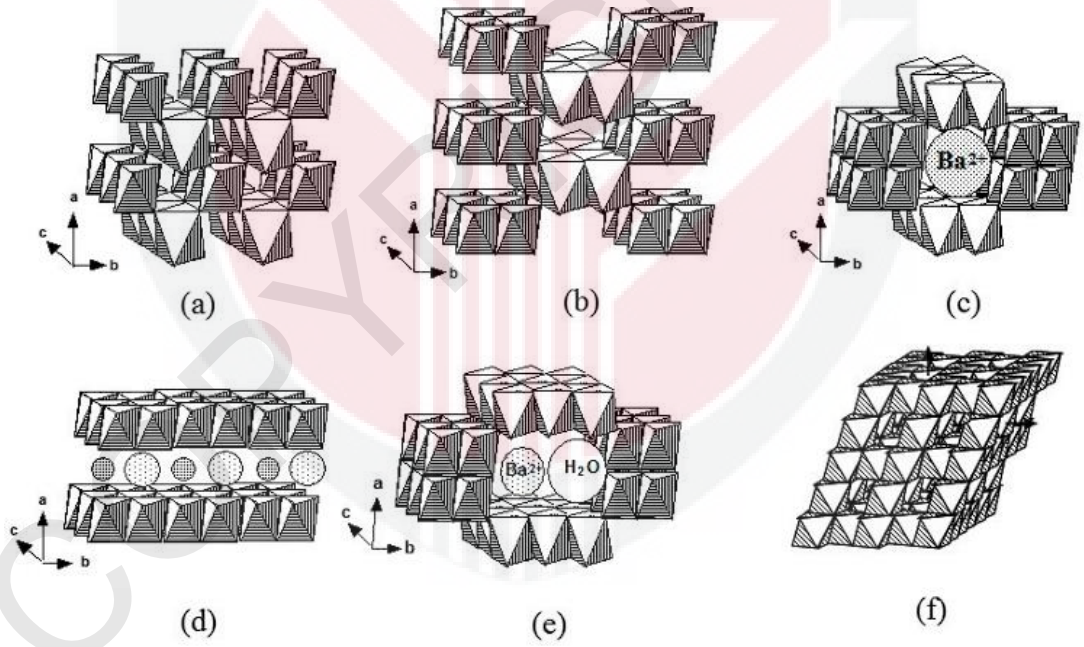

Figure 2.2. Representation of the different MnO_2 frameworks characterized by their tunnel (m × n) structures. (a) pyrolusite (1 × 1); (b) ramsdellite (1 × 2); (c) hollandite (2 × 2); (d) birnessite (1 × ∞); (e) romanechite (2 × 3); and (f) spinel (1 × 1). (Julien et al., 2017)

Table 2.1. Summary of crystallographic data of some manganese dioxide compounds.

Compound	Mineral	Crystal Symmetry	Features
α-MnO_2	Hollandite	Tetragonal (I4/m)	(2 x 2) tunnel
R-MnO_2	Ramsdellite	Orthorhombic (Pbnm)	(1 x 2) tunnel
β-MnO_2	Pyrolusite	Tetragonal ($P4_2/mnm$)	(1 x 1) tunnel
γ-MnO_2	Nsutite	Complex tunnel (hex.)	(1 x 1)/(1 x 2)
δ-MnO_2	Birnessite	Rhombihedral (R-3m)	$(1 \times \infty)$ layer
ε-MnO_2	Akhtenkite	Hexagonal (P63/mmc)	Dense stack
λ-MnO_2	Spinel	Cubic (Fd3m)	(1 x 1) tunnel
ψ-MnO_2	Psilomelane	Monoclinic (P2/m)	(2 x 3) tunnel
T-MnO_2	Todorokite	Monoclinic (P2/m)	(3 x 3) tunnel

With the tunnel size increasing from β-MnO_2 to α-MnO_2 and T-MnO_2, the structure gradually becomes heterogeneous, featuring a higher density of tunnel intergrowth resulting from [MnO_6] disordering. For β-MnO_2, [MnO_6] octahedra units are regularly patterned to form well-aligned (1 x 1) tunnels exclusively. For α-MnO_2, while most of the tunnels are well-aligned (2 x 2) tunnels, heterogeneous tunnel intergrowths of larger tunnels, such as (2 x 3) and (2 x 4) tunnels, were present. For T-MnO_2, while most tunnels are (3 x 3), a substantial number of heterogeneous tunnels with either smaller or larger sizes were observed. Interestingly, all these heterogeneous tunnels are aligned along certain crystal planes and exhibit a crystallographic relationship with the major tunnel phases (Yuan et al., 2019).

2.3 Synthesis of MnO_2 nanowires

Special attention has been address to the synthesis approach of the MnO_2. The morphology and electrochemical properties of MnO_2 strongly depend on the preparation process. The synthetic methods for nanostructured MnO_2 including simple reduction, coprecipitation, sol-gel, thermal decomposition, and the hydrothermal synthesis molten-salt method (Liu et al., 2013). Various nanostructured objects investigated over the years include nanowires, nanorods, nanoflowers, nanosheets, nanoflakes, nanotubes, nanourchins, nanospheres, nanobelts, nanodisk, and nanofibers.

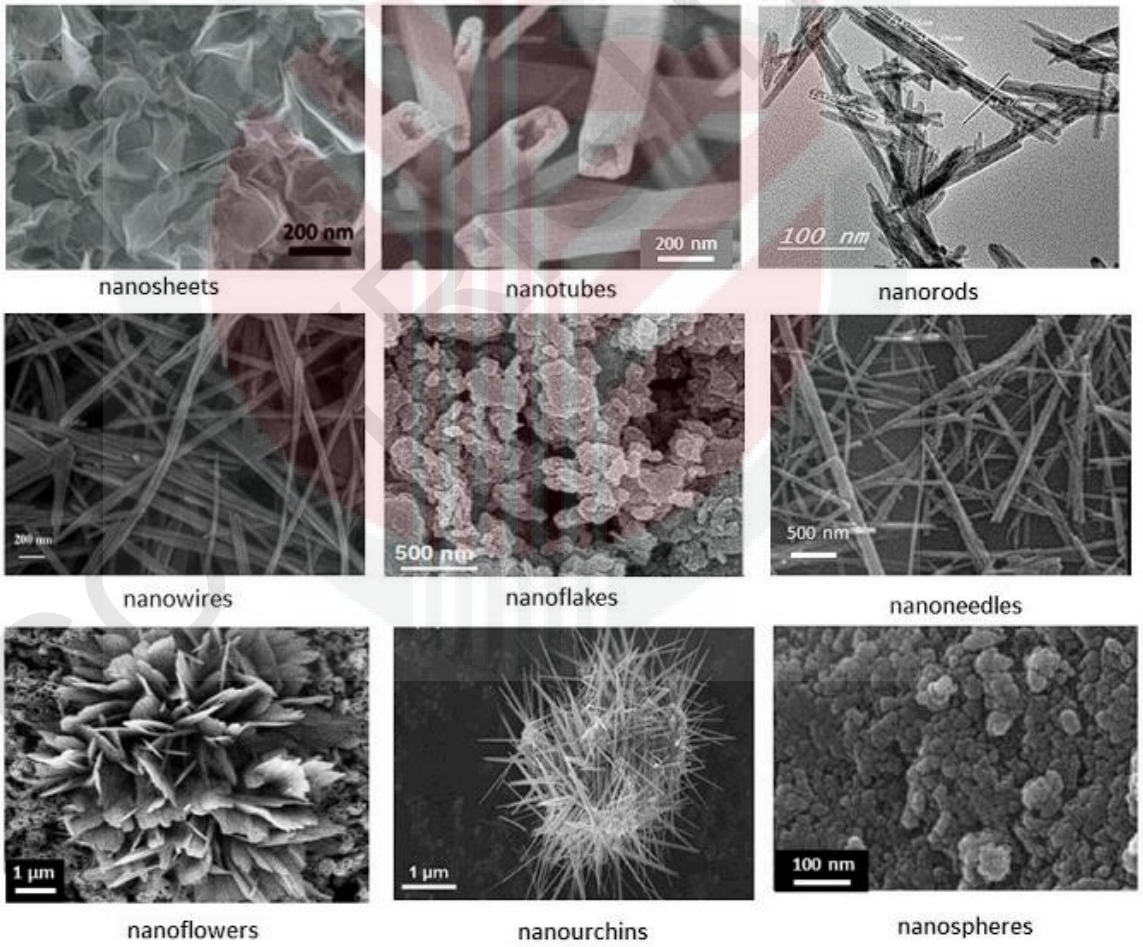

Figure 2.3. SEM images of the various nanostructured MnO_2 materials. These micrographs show the morphologies of the different MDO samples described in the text.

The various morphologies of nanostructure MnO_2 materials are illustrated by the SEM images in Figure 2.3. Based on classical synthesis, MDO are classically prepared by oxidation of aqueous Mn^{2+} solution using various oxidants such as MnO^{4-}, $S_2O_8^{2-}$, H_2O_2, O_3, ClO^{3-}, $Cr_2O_7^{2-}$, etc. It has been experimentally shown that the size and morphology of particles depend on the nature of the oxidant and the pH of the mixture.

2.3.1 Redox Reaction

The most popular route consists of the reduction of $KMnO_4$ by salts or organic substances. As an example, with manganese acetate as an oxidant of potassium permanganate, the simple redox reaction can be expressed by:

$$3Mn(CH_3COO)_2 + KMnO_4 + 2H_2O \rightarrow 5\ MnO2 + 4CH_3COOH + 2CH_3COOK$$

Hashem et al. (2013) synthesised two polymorph MnO_2 nanorods using redox reaction between $(NH_4)_2S_2O_8$ and $MnSO_4 \cdot 4H_2O$ for α-MnO2 and $(NH_4)_2S_2O_8$ and $Mn(NO_3)_2 \cdot 4H_2O$ for β-MnO_2. Rod-shaped structures of α-MnO_2 and β-MnO_2 are obtained. The diameters of these rods are in the range of 15 nm to 20 nm for α-MnO_2 and β-MnO_2 samples, respectively.

Yin et al. (2015) studied the effects of metal cations and protons on the structures and morphologies of MnO_2. K^+ and H^+ are competitive in solution to form: (i) cryptomelane α-MnO_2 is formed when the amount of K^+ is higher than the amount of H^+ ; (ii) for the growth of the pyrolusite structure β-MnO_2 occurs at a higher quantity of H^+ ; (iii) the layered phase δ-MnO_2 is obtained at a concentration of K^+ much greater than that of H^+. Liu et al. (2015) successfully prepared nanosheets with average of 1 nm thickness using a slow redox reaction between $KMnO_4$ and sodium dodecyl sulfate (SDS) in acidic medium (diluted H_2SO_4), in which SDS served as the precursor to reduce $KMnO_4$. Jeong and Manthiram mentioned the preparation of MnO_2 by the reduction of $KMnO_4$ using various inorganic reducing agents such as potassium borohydride, sodium dithionate, and sodium hypophosphite.

2.3.2 Hydrothermal Method

Hydrothermal synthesis is an efficient method for producing inorganic nanomaterials, and it potentially provides strong control of properties such as crystalline phase, particle size and morphology. In a typical hydrothermal synthesis of MnO_2, a reduction-oxidation reaction occurs where potassium permanganate ($KMnO_4$) is reduced using manganese sulfate ($MnSO_4$).

$$2K^+ + 2MnO_4^- + 3Mn^{2+} + 3SO_4^{2-} + 2H_2O \rightarrow 5MnO_2 + 2K^+ + SO_4^{2-} + 4H^+ + 2SO_4^{2-}$$

This reaction has been shown to produce α-, β- and δ-MnO_2 under hydrothermal and refluxing conditions. Previous studies on MnO_2 synthesis report needle shaped nanocrystals of α and β-MnO_2 and sheet-shaped δ-MnO_2 nanocrystals. However, the studies differ in their claims about how to control the crystalline phase like via pH, reaction time and temperature. One of the predominant ways to tune between formation of α-, β- and δ-MnO_2 is varying the fraction of potassium K^+ in the reaction solution. More potassium leads to the more open structure of δ-MnO_2, whereas intermediate potassium content gives α-MnO_2, and low amounts give β-MnO_2 (Wang et al., 2003 and Cheng et al., 2006).

2.4 NH_4F as Secondary Precursor

Precursor also influence the growth of MnO_2 nanostructure. A study from Cheng et al (2019) successfully synthesised $ZnCo_2O_4$ via a simple hydrothermal condition and a consequent annealing process. By adding NH_4F as precursor, a morphological transformation, higher surface area and higher specific capacitance was observed in $ZnCo_2O_4$ nanostructures. Furthermore, NH_4F is used as soluble inorganic salts to adjust the morphologies of metal oxide as surfactants or template agents because they are environmentally friendly, inexpensive and easy to obtain as compared to others organic additives.

The main reason for this phenomenon is speculated by them as following:

1. F^- anions could help form more active sites for nucleation and growth of the target materials and further benefit the compact adhesion
2. The pH value of the precursor solution (the pH value is 5.01) was influenced by the addition of NH_4F, which further affected the decomposition of precursor and the formation rate of the metal oxide precursor
3. The strong coordination of F^- anions with metal cations decreased the release speed of metal ions and further slowed down the nucleation rate of the metal oxide precursor

2.5 Formation Mechanism of MnO_2 nanowire

Birgisson et al. in their studies showed that three nanocrystalline phases, δ-, α- and β-MnO_2, are observed at different reaction temperature and time via hydrothermal synthesis. The results is tabulated as in Table 2.2.

Table 2.2. Crystal phase and stage of MnO_2 with varied temperature and reaction time

Temperature	Reaction Time	Crystal Phase	Stage
-	-	δ-MnO_2	-
200	40 minutes	α-MnO_2	-
225	10 minutes	α-MnO_2	Stage 1
225	15 minutes	α-MnO_2 and β-MnO_2	Stage 2
225	40 minutes	β-MnO_2	Stage 3
250	5 minutes	β-MnO_2	-

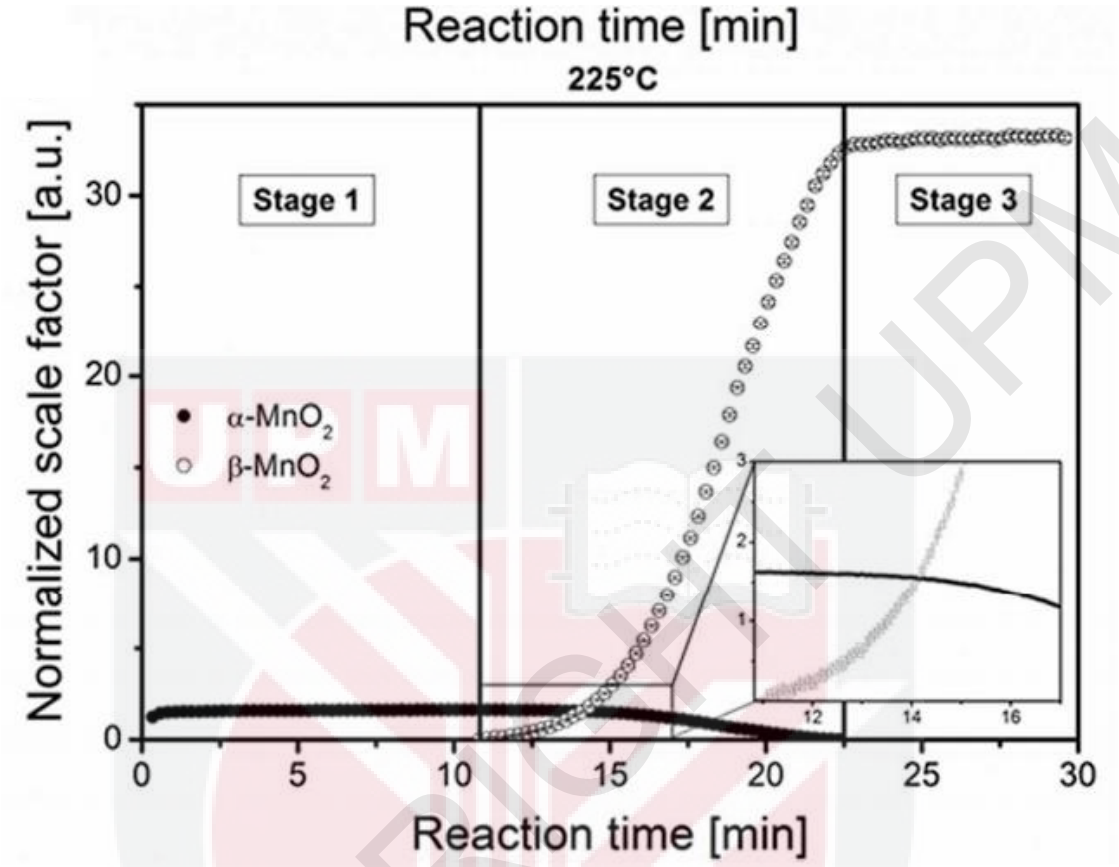

Figure 2.4. Refined scale factor normalised to chemical formula unit plotted as a function of reaction time for α- and β-MnO_2 at 225°C (Birgisson et al., 2018).

Phase transformation from α- to β-MnO_2 can be expected since β-MnO_2 is the thermodynamically most stable MnO_2 phase. Based on the time resolved data in Figure 2.4, the reaction can be divided into three separate stages. In the first stage, pure or almost pure α-MnO_2 is the only crystalline product. In stage two, α-MnO_2 transforms completely to β-MnO_2 and in stage three, pure β-MnO_2 is the only crystalline product. Phase transformation from α- to β-MnO_2 can be expected since β-MnO_2 is the most stable MnO_2 phase.

On **stage 1**, the weight of α-MnO_2 increases rapidly with a simultaneous decrease in the δ-MnO_2 until no δ-MnO_2 is detected in the reaction solution. The formation of the initial α-MnO_2 is roughly one to one with the disappearance of δ-MnO_2. Initial α-MnO_2 crystallites are formed through a direct transformation from the δ-MnO_2 crystallites. Then, δ-MnO_2 has disappeared and the weight fraction of α-MnO_2 increases slowly. During stage one the coherence length of δ-MnO_2 grows rapidly initial size in the precursor solution. After δ-MnO_2 has disappeared, the coherence length of α-MnO_2 keeps increasing slowly.

Formation of tunnelled MnO_2 structures from precursor containing layered δ-MnO_2 is common. Many different formation mechanisms, such as rolling of the layers; buckling, dissociation and recombination of the layers; and collapsing the layers into tunnels, have been proposed based on experimental and theoretical considerations (Wang et al., 2003). The initial α-MnO_2 crystallites are formed from the δ-MnO_2 crystallites, while further growth happens by inclusion of amorphous α-MnO_2. It therefore seems that the structural relationship between α- and δ-MnO_2 dictates that α-MnO_2 is formed in the reaction solution before β-MnO_2.

For **stage two**, the weight fraction for β-MnO_2 rises rapidly with a corresponding decrease of α-MnO_2. This leads to the amount of β-MnO_2 being high in the end of stage two than the amount of α-MnO_2. These observations show the transformation of α-MnO_2 crystallites into β-MnO_2 crystallites. Initially the β-MnO_2 crystallites size are slightly smaller than the α-MnO_2 crystallites. However, β-MnO_2 grows faster than α-MnO_2 meaning that they become equal in size. During the middle part of stage two both phases

have the same size, but then α-MnO_2 starts growing more rapidly. α- to β-MnO_2 phase transformation is a direct solid-state transformation and not a dissolution recrystallisation.

In the initial stage of reaction **stage three**, the weight fraction of β-MnO_2 grows rapidly corroborating the initial increase in crystallite volume. Later, slower growth of the β-MnO_2 in reaction stage three observed and here Ostwald ripening is a more likely growth mechanism than oriented attachment. The coherence length for β-MnO_2 refines throughout reaction stage three.

Wang et al. (2002) suggest that under hydrothermal conditions all the MnO_2 one-dimensional nanostructures have a common developing process, which is characteristic of a rolling mechanism and phase transformation. They proposed the possible mechanism of MnO_2 growth as follows:

1. Under hydrothermal conditions the MnO_x units will appear first in the solution, and then through a condensation reaction they will form sheets of δ-MnO_2.
2. The layer structure of δ-MnO_2 tends to curl with an elevated temperature and pressure. Some tubular structure may appear in the system.
3. The lamellar structure of MnO_2 is in a metastable state. If there are not enough cations, the layer structure will collapse.
4. Along with the phase transformation, the tubular and curling lamellar structures will grow into nanowires.

5. During the following hydrothermal process, the shorter nanowires may redissolve into the solution phase, and the longer ones grow into much longer ones.
6. The aspect ratios of the final products are determined by the ion concentration existing in the reaction system and the anisotropic nature of the corresponding crystal structures.

CHAPTER 3

METHODOLOGY

3.1 Introduction

This chapter summarises the properties of the raw material and material preparation utilised in this project. The preparation of MnO_2 nanowires are prepared in a hydrothermal oven under different growth times which are 3, 5, 7 and 9 hours. The structural, electrical and morphological characterisation techniques used to examine the MnO_2 samples are also explained

3.2 Material properties

The materials used in the project are without any purification process. The solvent used in all preparation processes is deionised water. Deionised water has a resistivity of 18.2 MOhm.

3.2.1 Potassium permanganate, $KMnO_4$

The chemical formula of Potassium Permanganate is $KMnO_4$. It appears in a bright purple crystalline solid and odourless. The density of $KMnO_4$ is 2.70 g/cm^3, and it has a melting point of 240°C. Potassium permanganate is a potent oxidising agent which can react with a variety of chemical compounds. It possesses the highest ionic conductivity among other cations.

It is known generally that $KMnO_4$ is decomposed into potassium manganate and MnO_2, above 200°C in air, releasing oxygen. Peters et al. reported that the single steps of the thermal decompositions of $KMnO_4$, K_2MnO_4, and K_3MnO_4 were investigated by thermal analysis techniques. In case of $KMnO_4$, the decomposition is expressed simply as follows.

$KMnO_4 \rightarrow K_3MnO_4 + K_2MnO_4 + MnO_2 + O_2$

For the synthesis of MnO_2-based powders via single step thermal treatment, $KMnO_4$ was selected due to its slow decompose rate.

Figure 3.1 $KMnO_4$ Chemical Structure

3.2.2 Ammonium fluoride, NH_4F

The chemical formula of ammonium fluoride is NH_4F. It exists in a white crystalline solid and odourless. It has a density of 1.01 g/cm^3 and a melting point of 238 °C. The function of ammonium fluoride is used as a buffer solution to control the pH condition in a crystal growth system.

Figure 3.2 NH_4F chemical structure

3.3 Preparation of MnO_2 in different growth time

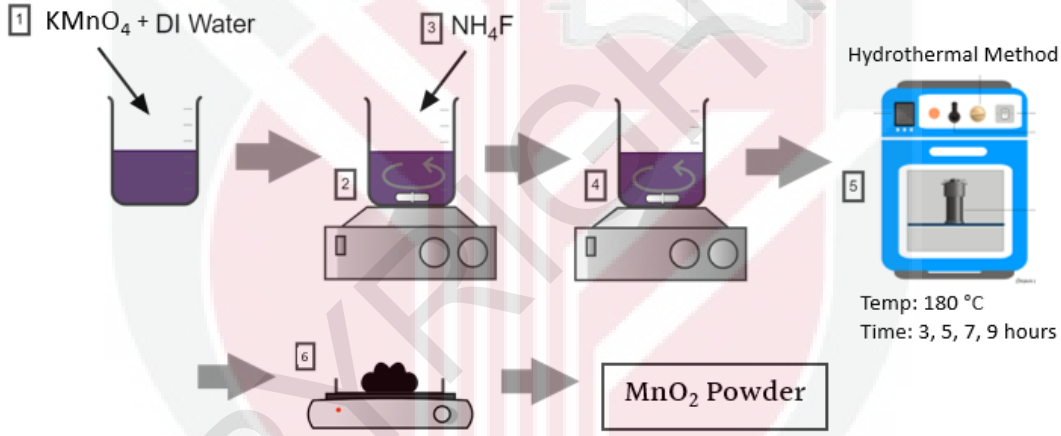

Figure 3.3 Preparation step of MnO_2

Homogenous MnO_2 nanowires were prepared via wet-chemical synthesis approach. Firstly, 158.0 mg of the potassium permanganate, $KMnO_4$ (Sigma Aldrich, 99%, reagent grade) were measured and dissolved in 25 ml of deionised water. The solution was stirred at 250 rpm for 15 minutes. This process was used to produce a homogenous solution. Secondly, 37.0 mg of the ammonia fluoride, NH_4F (Eluka, 99%) was added to the solution and was stirred at 250 rpm for 15 minutes. The ammonia fluoride, NH_4F, acts as a buffer

solution to control the pH value in the crystal growth system. Next, the solution was inserted into the Teflon autoclave chamber and heated for 3 hours at 180°C in a conventional hydrothermal oven. All steps were repeated with different heating times at 5 hours, 7 hours and 9 hours. Finally, four samples with different growth times were collected and dried at 60˚C for overnight to obtain a fine powder.

3.4 Sample characterisation

There are several characteristics used to investigate the structural, morphology and electrical properties of MnO_2 samples.

3.4.1 X-ray diffraction (XRD)

X-ray diffraction (XRD) is a technique used in materials science to determine the structural properties of unknown compounds. It is operated by irradiating a sample with incident X-rays. The diffraction intensity and scattering angles of the material is obtained from this technique (Alamgir, 2021).

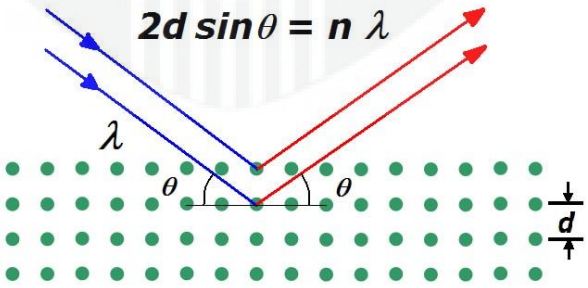

Figure 3.4: X-ray diffraction schematic diagram.

The intensity of the X-rays reflected was reported from the detector. Successive interference happens when an incident X-ray geometry directly impacts on the sample. The diffraction must always obey the Bragg Law:

$$2d \sin \theta = n\lambda$$

Later, the X-ray signal is captured and analysed by the detector, which transforms the signal to the count rate. The sample preparation steps for the XRD is described as follow:

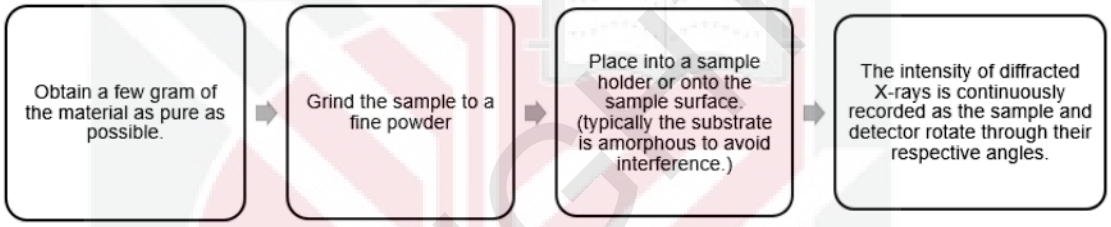

Figure 3.5 The sample preparation for x-rat diffraction analysis. (Source: Afiqah, 2020)

3.4.2 Raman spectroscopy

Raman Spectroscopy is a non-destructive analysis technique that provides detailed information about chemical structure, phase and molecular interactions. It is based upon the interaction of light with the chemical bonds within a material.

Raman is a light scattering technique whereby a molecule scatters incident light from a high-intensity laser light source. Most of the scattered light or Rayleigh Scatter is at the same wavelength as the laser source and does not provide useful information. However, a small amount of light is scattered at different wavelengths, which depend on the chemical structure of the analyte – this is called Raman Scatter (Adar, 2014).

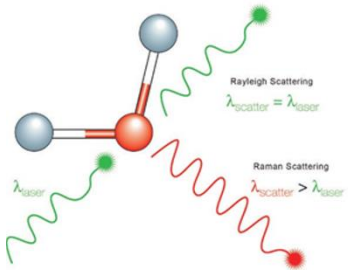

Figure 3.6 Raman principle. (Source: Horiba, 2018)

A Raman spectrum features several peaks, showing the intensity and wavelength position of the Raman scattered light. Each peak corresponds to a specific molecular bond vibration, including individual bonds and groups of bonds.

Raman spectroscopy is not a primary structural technique such as x-ray diffraction. Therefore, the well-crystallised sample must be prepared. During the experiment, MnO_2 powders were pressed into a film to achieve a mirror-like surface sample for Raman analysis. The sample preparation for Raman spectroscopy was shown in Figure 3.7.

Figure 3.7 Sample preparation for Raman spectroscopy. (Source: Afiqah, 2020)

3.4.3 Field-emission scanning electron microscopy (FESEM)

Field-emission scanning electron microscopy (FESEM) is used to provide the morphological information of the samples. In FESEM, the phenomenon of field electron

emission was used to obtain an image on the detector on the basis of the difference in the work function of the various crystallographic planes on the surface. A field-emission cathode in the electron gun of a scanning electron microscope provides narrower probing beams at low as well as high electron energy, resulting in both improved spatial resolution and minimised sample charging and damage (PhotoMetrics Inc).

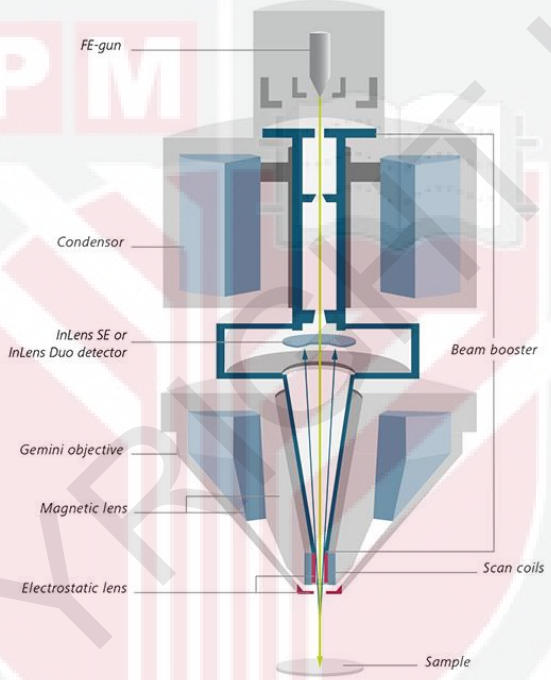

Figure 3.8 Schematic cross-section of FESEM. (Source: Gemini Technology, 2019)

In the vacuum chamber, the electrons are released from the ground emission source and stimulated to a strong electrical field. After that, the primary electrons are guided and deflected by electronic lenses to create a narrow scan beam that accelerates the target materials. Therefore, secondary electrons are released from the sample and detected by a detector. Finally, the electrical signal is amplified and transmitted to a computer or digital

image for recording purpose. The sample preparation for FESEM analysis is summarised as follow: -

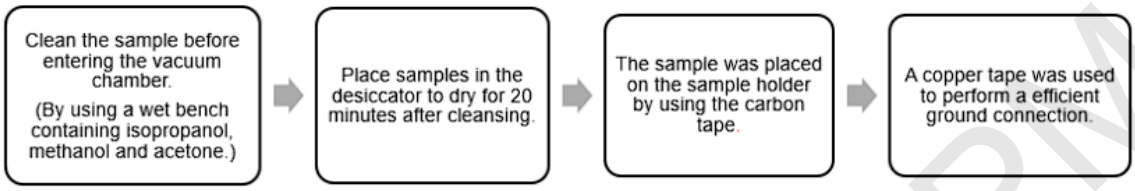

Figure 3.9 Sample preparation for FESEM. (Source: Afiqah, 2020)

3.4.4 Four-point probe analysis (4PP)

Four-point probe measurer (4PP) is a tool that is commonly used to measure the resistivity value of a thin layer of electronic material

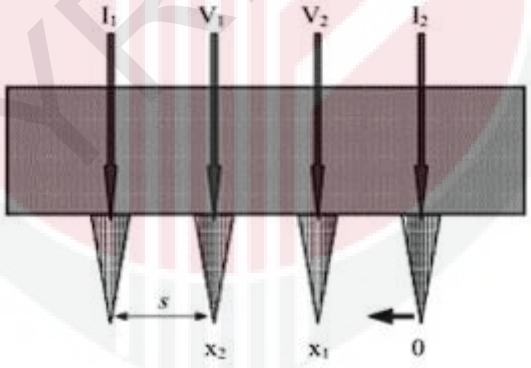

Figure 3.10 FPP Scheme. (Source: Waremra & Betaubun., 2018)

This measurer can be conducted via to type of set up which is in 4 probes and 2 probes. During this operation, the outermost two cantilever probe is supply with I=2A current whereas the inner two cantilever probe is used to measure the potential different on the selected point of the measured material.

$$\rho = \frac{\pi t}{\ln 2} \frac{V}{I}$$

These four points are joined in a straight line, with the spacing between the probes arranged so that each of the probes has the same distance. Two external probes provide a steady electrical current through the sample. The voltage decreases when there is a resistance value recorded from the sample (Waremra & Betaubun., 2018). The sample preparation technique in 4PP is summarised in Figure 3.

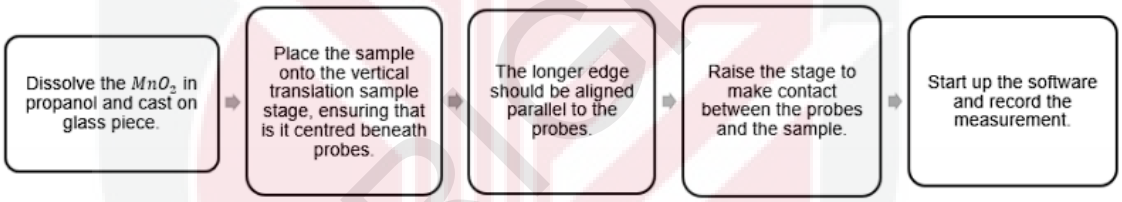

Figure 3.11 Sample preparation for 4PP. (Source: Afiqah, 2020)

CHAPTER 4

RESULT AND DISCUSSION

4.1 Introduction

The results and findings obtained in this research are discussed in this chapter. Four detailed data analysis related to the morphology, crystal structure, structural analysis and electrical properties of MnO_2 nanowires are included in this chapter. There are four sample characterisation are conducted which are electron microscopy (FESEM), Raman analysis, X-ray diffraction (XRD) analysis and Four Point Probe (4PP) analysis. In addition, this chapter also discusses the growth mechanisms of MnO_2 nanowires.

4.2 Morphological Analysis

The morphology of MnO_2 nanowires was examined using the Field Emission Electron Scanning Microscopy (FESEM) at the accelerating voltage of 3 keV. The magnification was set at 10 kX for low magnification and 30 kX for high magnification. Figure 4.1(a-h) shows the images at low and high magnifications, respectively. In general, hydrothermal synthesis of tunnel structured MnO_2 produces nanoparticles with a one-dimensional shape, such as nanorods and nanowires. FESEM images of the produced tunnel phases show nanowires shape for α-MnO_2 and β-MnO_2, which is consistent with the literature (Byles et al., 2018).

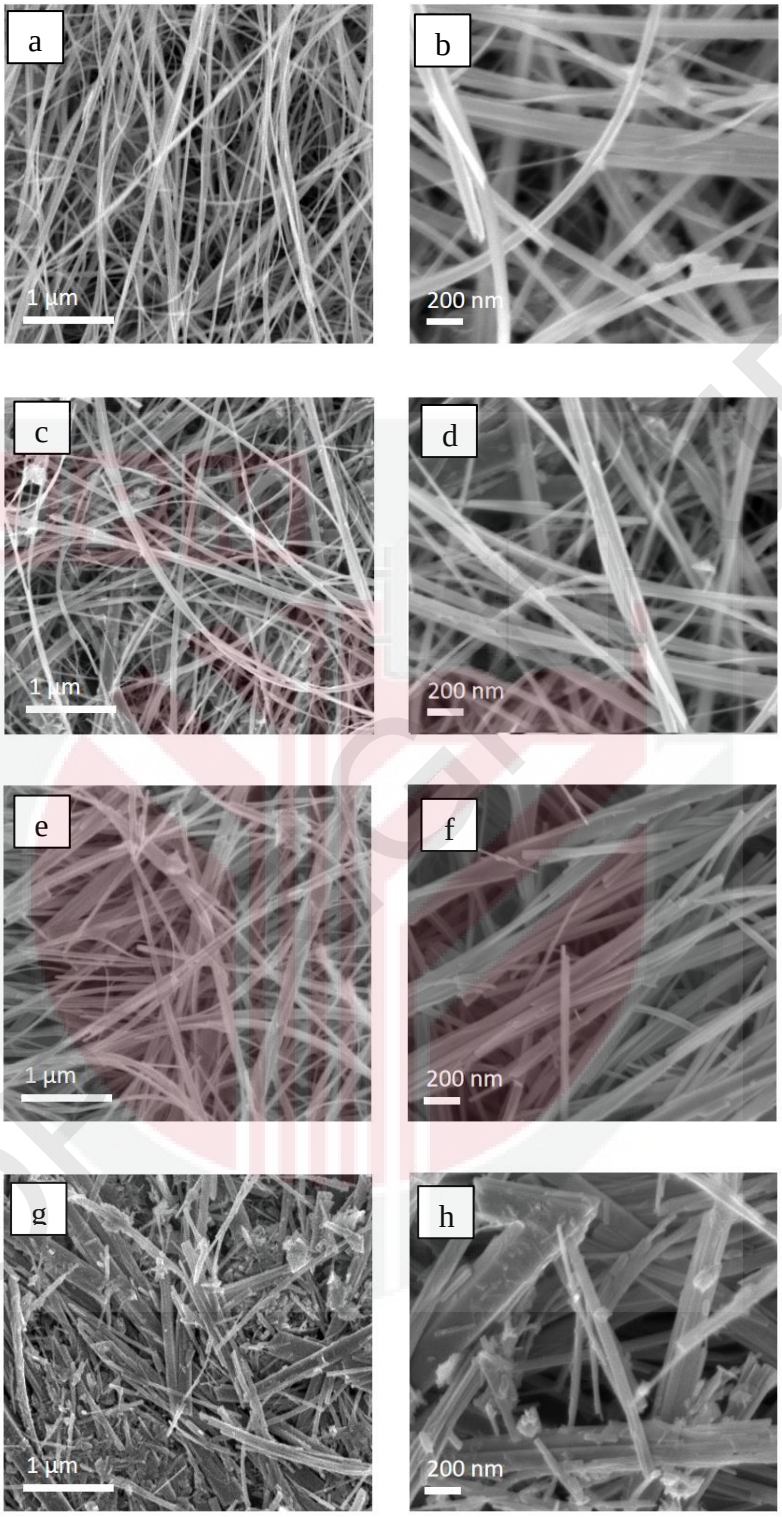

Figure 4.1. FESEM morphologies of (a-b) MnO_2-3H, (c-d) MnO_2-5H, (e-f) MnO_2-7H, and (g-h) MnO_2-9H at low and high magnification, separately.

Figure 4.1(a-b) show the FESEM images of 3- hours hydrothermal treatment samples and label as MnO_2-3H. The sample obtained in nanowires with diameters about (37 ± 10) nm. The length of the nanowires is in micrometer range. All these measurements were determined using an ImageJ software. The nanowires are thin, flexible, and well dispersed. For MnO_2-5H, the diameter of the nanowire increases to (48 ± 13) nm. Some of the nanowires started to combine with each other. There are some agglomerated nanoparticles initially form at this stage (Figure 4.1(c-d)). For the sample MnO_2-7H, the nanowire continues larger diameter of (71 ± 27nm). The nanowire became solid and less flexible. An agglomerated nanoparticles also become bigger and obviously seen at Figure 4.1(e-f). Lastly, for MnO_2-9H, the sample transform drastically from a uniform nanowire to a broad size of MnO_2 nanorod with diameter of (76 ± 34) nm.

Table 4.1 depict the sample information from FESEM analysis. It can be concluded that by increasing the hydrothermal treatment time, the nanowires become thicker in diameter, shorter in length, less flexible nanowire, increasing size and quantity of agglomerated nanoparticles.

Table 4.1 MnO_2 sample nanostructures and the diameters

Growth Time (h)	**Diameter, d (nm)**
3	37 ± 10
5	48 ± 13
7	71 ± 27
9	76 ± 34

4.3 Growth Mechanism of MnO_2 nanowires

Figure 4.2 depicts an illustration of the proposed formation mechanism of MnO_2 nanowires. It can be summarised into two important stages, namely (i) a nucleation process and (ii) crystal growth process. Stage 1 describes the dissociation of $KMnO_4$ and NH_3F at the early stage of the process. When $KMnO_4$ and NH_4F are dissolved in deionized water, it forms a free-moving ion that contains of K^+, MnO_4^-, NH_4^+, F^-. The NH_4^+ further undergoes a reduction process and further produced a OH^-, which acted as a reducing agent in MnO_4^-. By this process, the addition of NH_4F into the growth solution indirectly led to the increase of decomposition rate of MnO_4. Then, MnO_6 octahedral as the primary growth product was formed. The product will initialize the crystal growth process when the supersaturation stage is achieved. The chemical reactions can be described as follow: -

$$KMnO_4 + H_2O \rightarrow K^+(aq) + MnO4^-(aq)$$

$$NH_4F \rightarrow NH_4^+(aq) + F^-(aq)$$

$$F^- + H_2O \rightarrow HF + OH^-$$

$$MnO_4^- + 4H^+ + 3e^- \rightarrow MnO_2 + H_2O$$

$$MnO_4^- + F^- + NH_4^+ \rightarrow MnO_2 + HF + H_2O$$

Next, the nuclei will start to self-assembled and keep aggregated to form a small particles before the crystallization. At 3h of reaction time, a pure (2×2) α-MnO_2 nanowires is formed as agreed to the XRD data. In the intermediated concentration of K^+, it is strongly believe that the K^+ will predominantly intercalate into the tunnel framework of (1×1) β-

MnO_2 and later transformed to the tetragonal (2 × 2) α-MnO_2. Next, the nanowires go through dissolution-crystallisation process and oriented attachment process which make the nanowire to become thicker and attach to each other which driven by the reduction of the overall surface energy(Yuan et al., 2016). When the growth time further increases to 9 h, a truncated nanorod was formed owing to the deintercalation of K^+ from the tunnel to the mixture. This process lead to the phase transformation in domain MnO_2 crystal, which will be discussed in XRD analysis.

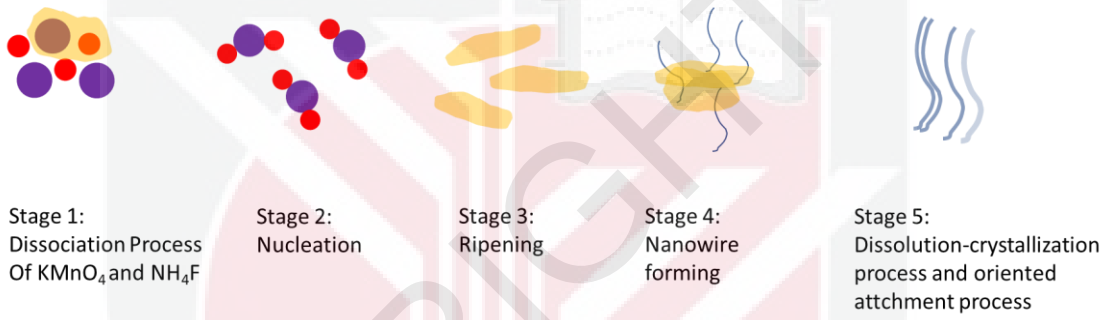

Figure 4.2 MnO_2 nanowires mechanism scheme

4.4 MnO_2 Structural Analysis

X-ray diffractometer (XRD) was used to characterize the crystalline structure of the samples. The diffraction pattern of samples synthesized at 180 ºC for 3, 5, 7 and 9 hours was plotted in Figure 4.3. The analysis was conducted at the scanning angle, 2θ of 20º to 60º under the CuKα irradiation source with wavelength of (0.154 nm). Figure 4.3 depicted the XRD patterns for all the prepared MnO_2 samples at various reaction times. The XRD patterns in Figures 4.3 can be indexed to a tetragonal α-MnO_2 [space group: 14/m (87)]

with lattice constants a=9.788Å and c=2.865Å (COD 96-151-4117), β-MnO_2 [space group: P 42/m n m (136)] with lattice constants a=4.400Å and c=2.870Å (COD 96-151-4111) and a cubic λ-MnO_2 [space group: Fd -3m (227)] with lattice constants a=8.097Å (COD 96-151-4234). Furthermore, there are additional peak which is refer to the source material peak of $KMnO_4$ that coming from excessive secondary by product.

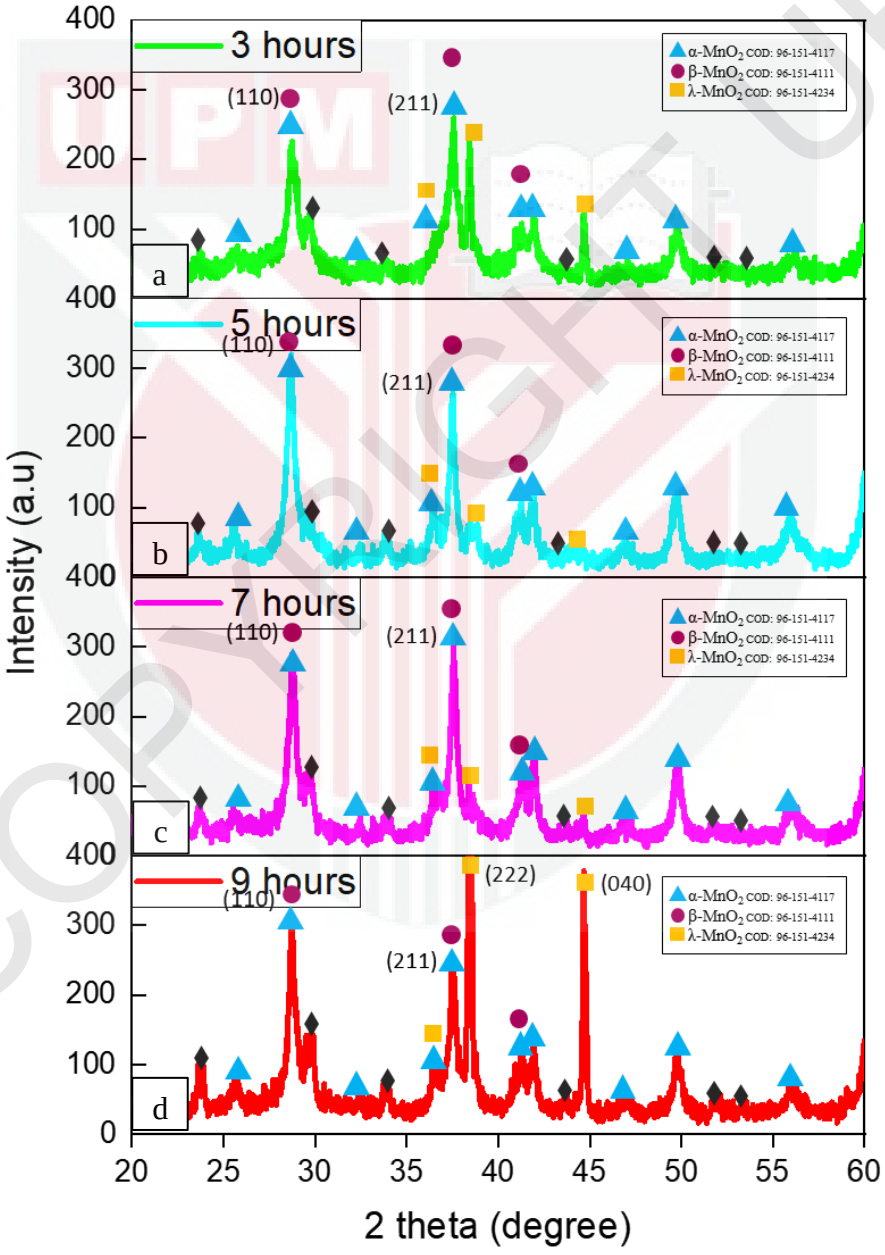

Figure 4.3 X-ray diffraction pattern of MnO_2 Nanowires.

Tabel 4.2 Results for (211) peak in different growth time

Growth Time, (h)	2θ (°)	FWHM	Crystalite Size (211), (nm)
3	37.47	0.24	34.96
5	37.49	0.34	24.97
7	37.54	0.29	29.13
9	37.45	0.19	43.69

From Figure 4.3(a), there are 18 diffraction patterns was detected at 23.7°, 25.7°, 28.7°, 29.7°, 32.5°, 33.8°, 36.7°, 37.5°, 38.4°, 41.2°, 41.9°, 43.6°, 44.7°, 47.1°, 52.4°, 53.5° and 56.0° which can be indexed to 3 different phases of MnO_2. The sharp and narrow diffraction peaks showed the high crystallinity of α-MnO_2 material (Shah et al., 2018). The MnO_2 growth at 3h showed the highest diffraction peak at 2θ of 37.47° with the value of FWHM of 0.24. This peak was referred to the (211) plane in MnO_2 crystal system. The crystalline size of MnO_2 was further calculated by using the Debye Scherrer equation and recorded as 34.96 nm (Xi et al., 2017). This result is consistent with the literature showing that α-MnO_2 is predominantly formed via hydrothermal growth approach.

When the growth time increase to 5 h, there are several changes in the diffraction pattern. For sample growth at 5 hours, the (211) peak shift to the highest diffraction angle and the FWHM was found to be increased to 0.34. There are three new peaks were found and can be indexed to λ-MnO_2. A dominant (040) plane of cubic MnO_2 phase was appeared at 38.44°. A further increase of growth time to 9 h had lead to the dominantly form λ-MnO_2. This can be observed from the intense peaks at the diffraction pattern of (222).

Figure 4.4 shows the compound quantification for all of the samples. The analysis is conducted using a Highscore analyser. When the growth time increased from 3 hours to 7 hours, the percentage of α-MnO_2 is increase from 54 to 69, meanwhile the β-MnO_2 and λ-MnO_2 decreased. These results signify the phase transformation process in polymorph MnO_2. When the growth time further increased to 9 hours, the percentage of λ-MnO_2 was found increased to 42 in contrast to the decreasing of α-MnO_2 and β-MnO_2 phase which are 41% and 17%. This result is consistent with the intense of (222) plane found in the diffraction pattern of MnO_2 grown at 9 h.

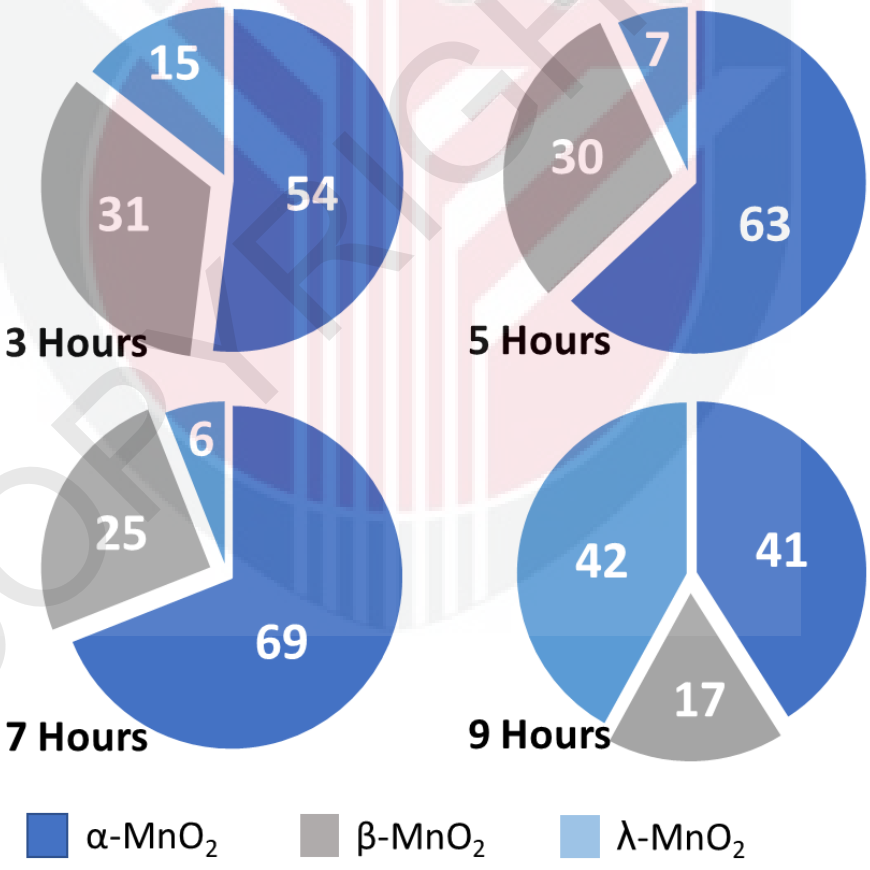

Figure 4.4 Phase quantification percentage for each phase

4.5 Molecular Structure Analysis

Raman spectroscopy analysis was used to study the molecular structure of MnO_2 nanowires. Raman analysis was carried out using the excitation wavelength of 452.5 nm with the power of 5W and signal resolution of 0.5 cm^{-1}. The result was plotted from 100 cm^{-1} to 3400 cm^{-1} as depicted in Figure 4.5. The prominent Raman peak for MnO_2-3H, MnO_2-5H, MnO_2-7H and MnO_2-9H were observed at 632.95, 634.99, 635.45 and 633.02 cm^{-1}. All of these peaks can be denoted to B_{2g} peaks. The sharp peak is attributed to symmetric Mn-O stretch of the primary linked MnO_6 octahedral. The arrangement of α-MnO_2 consists of double chain of edge-sharing [MnO_6] octahedral, which forming a (2 x 2) and (1 x 1) tunnel structures. The size of the (2 x 2) and (1 x 1) tunnels are 0.46nm and 0.189nm, respectively (Young et al., 2014). This result is quite consistent and compliant with the XRD result, proving MnO_2 as our only final product in the sample is successfully prepared.

When the growth time increased from 3h to 7h, it was observed that the peak is increased by 2.5 cm^{-1}, which are from 632.95 cm^{-1} to 635.45 cm^{-1}. The further increases growth time to 9 h had leading to a decreased of B_{2g} peaks by 2.43 cm^{-1}. This result indicated a shorter molecular chain was found in the 9h MnO_2. This finding is relevant to the molecular bond structure of λ-MnO_2 with a shorter bond length of 230 pm as compared to α-MnO_2 with 460 pm. Furthermore, the area under the curve of B_{2g} was analysed and tabulated in Table 4.3. From the analysis, it is found that the area under the curve was decreased when the growth time increased to 5 h. This result indicated that a bond shrinks at α-MnO_2. To attain

the stability in molecular structure, the sample underwent a phase transformation to β-MnO_2 and causing the decreasing in area under the peaks. When the growth time further increase to 7h, the area under the peaks is increasing to 35778, which is similar to 3h grown sample. This occurrence could be due to the deintercalation of K^+ into the molecular tunnel. A further increasing growth time at 9h had increased the area.

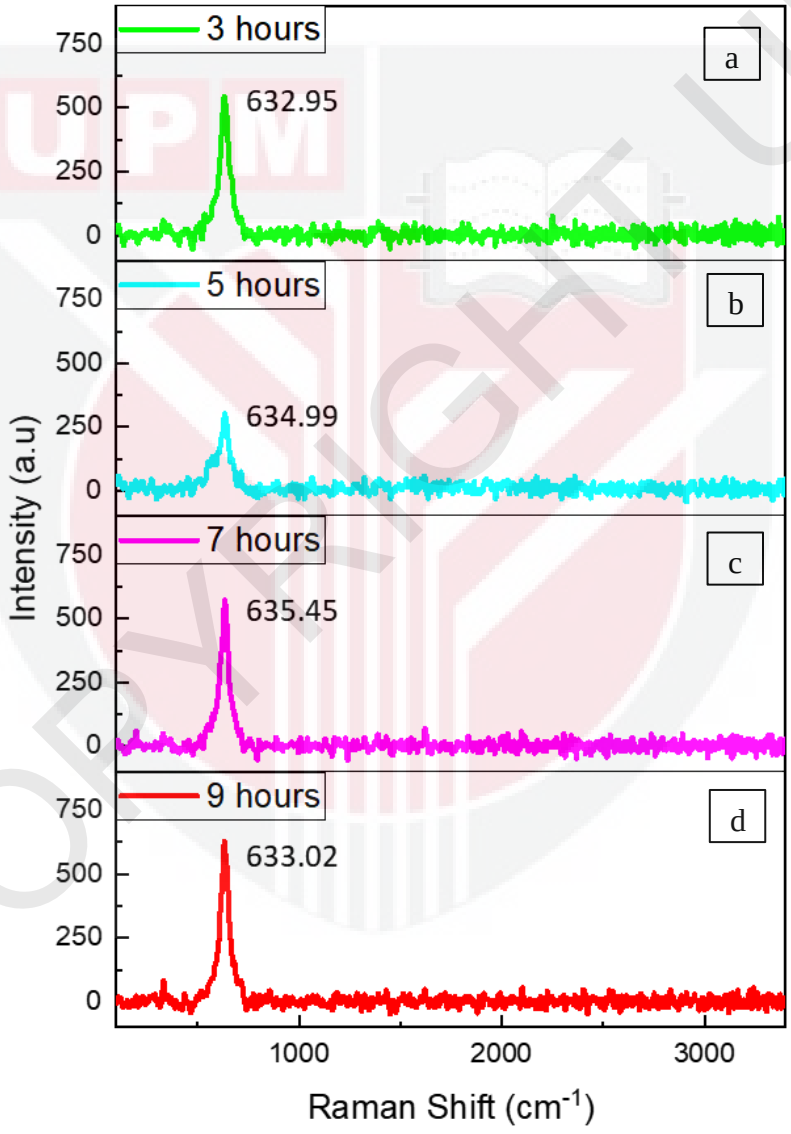

Figure 4.5 Raman spectra of MnO_2 nanowires samples

Table 4.3 Results for Raman Shift in different growth time

Growth Time (h)	Raman Shift (cm^{-1})	FWHM	Area under peak (cm^3)
3	632.95	57.30	36958.7
5	634.99	39.52	21570.8
7	635.45	38.60	35778.0
9	633.02	38.54	40343.7

4.6 Electrical Analysis

4-point probe analysis is used to measure the electrical properties of the samples. By using equation below, sheet resistance and the conductivity of the sample can be calculated. The result was summarized in Table 4.4 and Figure 4.6.

$$\rho = \frac{\pi t}{\ln 2}\frac{V}{I}$$

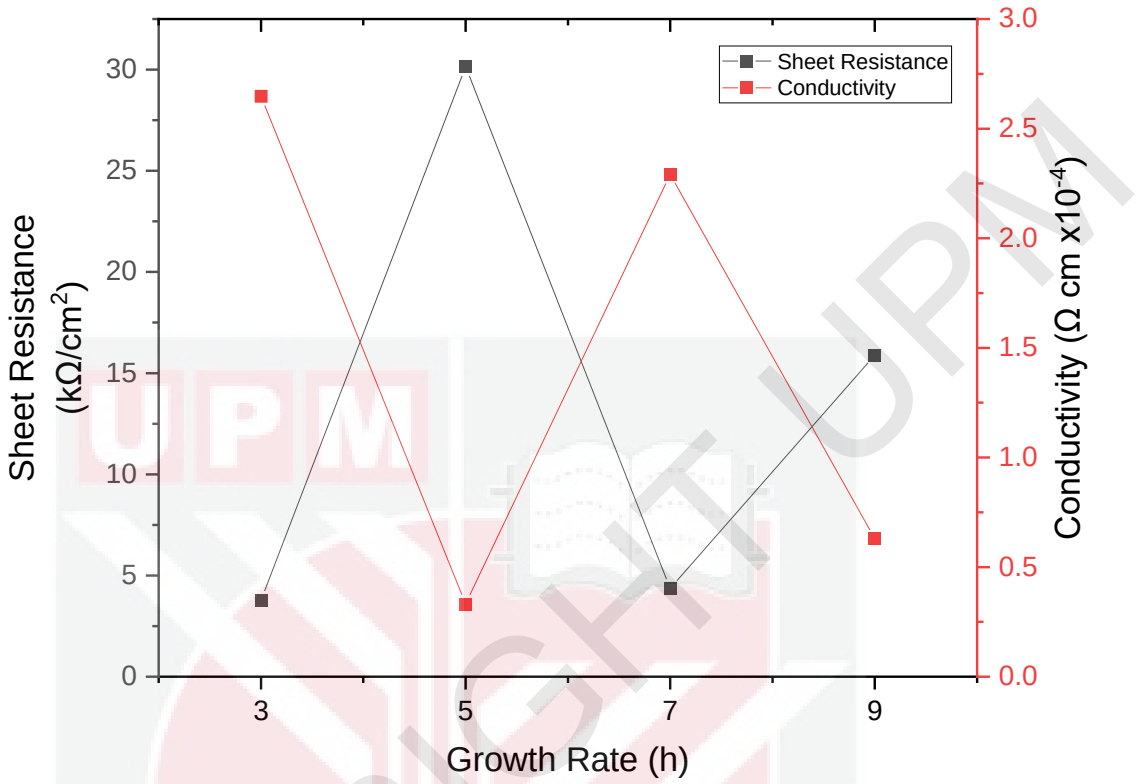

Figure 4.6 MnO_2 sample sheet resistance and conductivity graph

From Table 4.4 and Figure 4.6, the sheet resistance and the conductivity for the sample is depend on its molecular phase. It also shows that the conductivity of the sample is inversely proportional to sheet resistance. The conductivity of MnO_2-3H recorded a highest value at 2.65 $x10^{-4}$Ωcm. For MnO_2-5H sample, the conductivity decreased significantly to 0.33 $x10^{-4}$ Ωcm. The conductivity of MnO_2-7H sample was later increased to 2.29 $x10^{-4}$ Ωcm and further decreased to 0.63 $x10^{-4}$ Ωcm when the growth time increased to 9h. The fluctuation is coming from different electrical capabilities for difference phase for each of the sample (Yuan, Liu, et al., 2019).

Table 4.4 MnO_2 samples sheet resistance and conductivity

Growth Time (h)	Sheet Resistance ($k\Omega/cm^2$)	Conductivity ($\Omega cm \times 10^{-4}$)
3	3.78	2.65
5	30.15	0.33
7	4.36	2.29
9	15.88	0.62

Among the sample, MnO_2-3H recorded as a highest conductive sample. This could be related to two common factors, which are (i) the existence of α-phases and (ii) the quantification percentage of different polymorph phases. Its worth mentioned that different crystal phases have a different bond strength which might affect the molecular interaction with another existing crystal during a crystal formation. As prescribed from the XRD analysis, MnO_2-3H consisted of 2 different phases which are 65% of (2x2) α-MnO_2 and 35% of (1x1) β-MnO_2. The literature had mentioned that the (2x2) tunnel of α-MnO_2 presented a best electrical conductivity dure to its higher atomic packing fraction. In another note, the sample prepared at a highest growth time of 5, 7 and 9 hours showed a lowest conductivity, which can be due to the existence of shorter chain of , (1x1) cubic λ-MnO_2 .

CHAPTER 5

CONCLUSION

5.1 Introduction

In summary, the objectives of the present thesis have been successfully achieved. The general idea of MnO_2 nanowires and the achievement obtained in the results of the project was summarised. This chapter also includes some recommendation for future recommendation to improve the performance in supercapacitor devices.

5.2 Summarisation of The Research Study

MnO_2 is recognised as one of the outstanding materials that is commonly used in the green energy storage devices, due to its polymorphic nature. However, the detail understanding in the phase transformation mechanism and properties modification of this material is remain uncertain. There are many factors that effect the mechanism and properties of MnO_2 synthesis such as synthesis method, precursors, growth time, and the acidity of the substance.

This research aims to study the structural, morphological and electrical properties of MnO_2 nanowires under four different growth time in the hydrothermal oven, which is 3, 5, 7 and 9h treatment time. A few characterizations were done such as FESEM, XRD, Raman Spectroscopy and 4PP analysis to achieve the research objective.

FESEM characterization shows that the morphology of MnO_2 is existed in the nanowires structure. The nanowires are homogenously distributed on the carbon tape. As the growth time increase, the nanowire become thicker and less flexible. Furthermore, a small amount of MnO_2 nanoparticles that aggregates also increase and become bigger as the growth time increase. From the FESEM images, it can be concluded that the MnO_2 nanowires are existed in all of the samples.

Raman analysis was performed to study the molecular structure of the sample. The prominent Raman peak was observed at 632.95 cm^{-1} for MnO_2-3H sample which can be attributed to the symmetric Mn-O stretching bond of the linked MnO_6 octahedra. When the growth time increased, there is no Raman shift was observed indicated the stability of MnO_2 nanowires. At 7 hours, the peak is shifted by 2.5 cm^{-1} to a larger wavenumber which are from 632.95 cm^{-1} to 635.45 cm^{-1} and decreased by 2.43 cm^{-1} when the growth time further increased to 9 hours.

XRD analysis was conducted to study the crystal phase and the in-depth purity of the sample. From the XRD analysis, it is observed that the sample can be indexed to three different crystal phases of MnO2 which are (i) a pure (2x2) tetragonal α-MnO_2, (ii) (1x1) tetragonal β-MnO_2 and (iii) (1x1) cubic λ-MnO_2. The quantification percentage of crystal phases is changed when the growth time increased. From 3 hours to 7 hours, the MnO_2 samples majorly existed in the α-MnO_2 phase. At 9 hours, the crystal structure of MnO_2 is favorable in λ-MnO_2.

The electrical properties for all of the samples were measured using 4PP analysis. The conductivity of MnO_2 is strongly dependent on its crystal phases. The conductivity of MnO_2-3H recorded the highest value at 2.65 $x10^{-4}\Omega cm$. When the growth time increased to 5h, the conductivity decreased to the lowest conductivity of 0.33 $x10^{-4}\Omega cm$. For MnO_2-7H, the conductivity increased to 2.29 $x10^{-4}\Omega cm$ whereas MnO_2-9H possess a conductivity at 0.63 $x10^{-4}\Omega cm$.

Lastly, it is highly postulate that the dissolution-crystallization process and oriented attachment process play the main role in the formation mechanism of MnO_2 nanowires.

5.3 Conclusion

In conclusion, all the objectives in this research has been achieved. MnO_2 nanowires have been synthesised by the hydrothermal method. The effect of different growth time on structural, morphology and electrical properties of MnO_2 nanowires were successfully investigated. A detail crystal growth mechanism of MnO2 in the function of different growth time was successfully postulated.

5.4 Future Works

Even though the objectives are successfully achieved, a few suggestions can be made to improve future study. They are:

1. As MnO_2 have a good potential in their electrochemical properties, further this study by using MnO_2 as part of supercapacitor electrode device

material. Supercapacitor are expected to play an essential role in energy storage.

2. Perform EDX analysis to confirm the composition and quantification of MnO_2 nanowires.
3. Perform a closer and precise atomic imaging such as High-Angle Annular Dark-Field (HAADF) imaging and Annular Bright Field (ABF) imaging to learn more accurate morphological and structural analysis of MnO_2 sample.
4. Apply different volume or concentration of NH_4F to study the acidity effect on MnO_2 sample properties.

REFERENCES

Adar, F. (2014). Raman Spectra of Metal Oxides. *Spectroscopy*, *29*(10). https://www.spectroscopyonline.com/view/raman-spectra-metal-oxides

Afiqah, N. (2021). *Synthesis And Characterisation Of Manganese Dioxide Nanowires Based Supercapacitor In Different Aqueous Electrolyte*. Bachelor Thesis, Universiti Putra Malaysia.

Alamgir, F. (2021). *X-ray Diffraction*. JoVE Science Education Database.

Birgisson, S., Saha, D., & Iversen, B. B. (2018). Formation Mechanisms of Nanocrystalline MnO2 Polymorphs under Hydrothermal Conditions. *Crystal Growth & Design*, *18*(2), 827–838. https://doi.org/10.1021/acs.cgd.7b01304

Byles, B., & Pomerantseva, E. (2018). Stabilization of Tunnel Manganese Oxide Electrodes in Li-Ion and Na-Ion Batteries. *ECS Meeting Abstracts*, *MA2018-01*(44), 2581–2581. https://doi.org/10.1149/ma2018-01/44/2581

Byles, B. W., Cullen, D. A., More, K. L., & Pomerantseva, E. (2018). Tunnel structured manganese oxide nanowires as redox active electrodes for hybrid capacitive deionization. *Nano Energy*, *44*, 476–488. https://doi.org/10.1016/J.NANOEN.2017.12.015

Cheng, F., Zhao, J., Song, W., Li, C., Ma, H., Chen, J., & Shen, P. (2006). Facile Controlled Synthesis of MnO2 Nanostructures of Novel Shapes and Their Application in Batteries. *Inorganic Chemistry*, *45*(5), 2038–2044. https://doi.org/10.1021/ic051715b

Cheng, L., Xu, M., Zhang, Q., Li, G., Chen, J., & Lou, Y. (2019). NH4F assisted and morphology-controlled fabrication of ZnCo2O4 nanostructures on Ni-foam for enhanced energy storage devices. *Journal of Alloys and Compounds*, *781*, 245–254. https://doi.org/10.1016/J.JALLCOM.2018.11.402

Ferreira, O. P., Otubo, L., Romano, R., & Alves, O. L. (2006). One-Dimensional Nanostructures from Layered Manganese Oxide. *Crystal Growth & Design*, *6*(2), 601–606. https://doi.org/10.1021/cg0503503

Gao, T., Fjellvåg, H., & Norby, P. (2009a). Structural and morphological evolution of β-MnO2nanorods during hydrothermal synthesis. *Nanotechnology*, *20*(5), 055610. https://doi.org/10.1088/0957-4484/20/5/055610

Gao, T., Fjellvåg, H., & Norby, P. (2009b). A comparison study on Raman scattering properties of α- and β-MnO2. *Analytica Chimica Acta*, *648*(2), 235–239. https://doi.org/10.1016/J.ACA.2009.06.059

Hashem, A. M., Abuzeid, H. M., Abdel-Latif, A. M., Abbas, H. M., Ehrenberg, H., Indris, S., Mauger, A., Groult, H., & Julien, C. M. (2013). MnO2 Nano-Rods Prepared by Redox Reaction as Cathodes in Lithium Batteries. *ECS Transactions*, *50*(24), 125–130. https://doi.org/10.1149/05024.0125ecst

Hatakeyama, T., Li, H., Okamoto, N. L., Shimokawa, K., Kawaguchi, T., Tanimura, H., Imashuku, S., Fichtner, M., & Ichitsubo, T. (2021). Accelerated Kinetics Revealing Metastable Pathways of Magnesiation-Induced Transformations in MnO2 Polymorphs. *Chemistry of Materials*, *33*(17), 6983–6996. https://doi.org/10.1021/acs.chemmater.1c02011

Hunter, J. C. (1981). Preparation of a new crystal form of manganese dioxide: λ-MnO2. *Journal of Solid State Chemistry*, *39*(2), 142–147. https://doi.org/10.1016/0022-4596(81)90323-6

Julien, C. M., & Mauger, A. (2017). Nanostructured MnO2 as Electrode Materials for Energy Storage. *Nanomaterials*, *7*(11). https://doi.org/10.3390/nano7110396

Kaur, H., Kaur, H., & Sharma, A. (2021). A review of recent advancement in superconductors. *Materials Today: Proceedings*, *37*(Part 2), 3612–3614. https://doi.org/10.1016/J.MATPR.2020.09.771

Khadijah, S. (2021). *Design Of Mos2-Mno2/C/Pvdf Based Glucose Sensor In Electronic Skin Application. Thesis Submitted to the Department of Physics*. Bachelor Thesis, Universiti Putra Malaysia.

Li, Z., Ding, Y., Xiong, Y., & Xie, Y. (2005). Rational Growth of Various α-MnO2 Hierarchical Structures and β-MnO2 Nanorods via a Homogeneous Catalytic Route. *Crystal Growth & Design*, *5*(5), 1953–1958. https://doi.org/10.1021/cg050221m

Liu, R., Zhou, H., Liu, J., Yao, Y., Huang, Z., Fu, C., & Kuang, Y. (2013). Preparation of Pd/MnO2-reduced graphene oxide nanocomposite for methanol electro-oxidation in alkaline media. *Electrochemistry Communications*, *26*(1), 63–66. https://doi.org/10.1016/J.ELECOM.2012.10.019

Liu, Z., Xu, K., Sun, H., & Yin, S. (2015). One-Step Synthesis of Single-Layer MnO2 Nanosheets with Multi-Role Sodium Dodecyl Sulfate for High-Performance Pseudocapacitors. *Small*, *11*(18), 2182–2191. https://doi.org/https://doi.org/10.1002/smll.201402222

Oyedotun, K. O., Mirghni, A. A., Fasakin, O., Tarimo, D. J., Mahmoud, B. A., & Manyala, N. (2021). Effect of growth-time on electrochemical performance of birnessite manganese oxide (δ-MnO2) as electrodes for supercapacitors: An insight into neutral aqueous electrolytes. *Journal of Energy Storage*, *36*, 102419. https://doi.org/10.1016/J.EST.2021.102419

Shah, H. U., Wang, F., Javed, M. S., Saleem, R., Nazir, M. S., Zhan, J., Khan, Z. U. H., Farooq, M. U., & Ali, S. (2018). Synthesis, characterization and electrochemical properties of α-MnO2 nanowires as electrode material for supercapacitors. *International Journal of Electrochemical Science*, *13*(7), 6426–6435. https://doi.org/10.20964/2018.07.48

Wang, Omomo, Y., Sakai, N., Fukuda, K., Nakai, I., Ebina, Y., Takada, K., Watanabe, M., & Sasaki, T. (2003). Fabrication and Characterization of Multilayer Ultrathin Films of Exfoliated MnO2 Nanosheets and Polycations. *Chemistry of Materials*, *15*(15), 2873–2878. https://doi.org/10.1021/cm034191r

Wang, X., & Li, Y. (2002). Selected-Control Hydrothermal Synthesis of α- and β-MnO2 Single Crystal Nanowires. *Journal of the American Chemical Society*, *124*(12), 2880–2881. https://doi.org/10.1021/ja0177105

Waremra, R. S., & Betaubun, P. (2018). Analysis of Electrical Properties Using the four point Probe Method. *E3S Web Conf.*, *73*. https://doi.org/10.1051/e3sconf/20187313019

Wei, M., Konishi, Y., Zhou, H., Sugihara, H., & Arakawa, H. (2005a). Synthesis of single-crystal manganese dioxide nanowires by a soft chemical process. *Nanotechnology*, *16*(2), 245–249. https://doi.org/10.1088/0957-4484/16/2/011

Wei, M., Konishi, Y., Zhou, H., Sugihara, H., & Arakawa, H. (2005b). Synthesis of single-crystal manganese dioxide nanowires by a soft chemical process. *Nanotechnology*, *16*(2), 245–249. https://doi.org/10.1088/0957-4484/16/2/011

Xi, S., Zhu, Y., Yang, Y., & Liu, Y. (2017). Direct Synthesis of MnO_2 Nanorods on Carbon Cloth as Flexible Supercapacitor Electrode. *Journal of Nanomaterials*, *2017*, 7340961. https://doi.org/10.1155/2017/7340961

Xue, L., Wu, Z. S., Ge, C., & Zhang, X. D. (2013). Ultralow-temperature hydrothermal synthesis of Zn–Mn spinel nanocrystals: Its defect spinel of λ-MnO2 prepared by a soft chemical method. *Materials Chemistry and Physics*, *138*(1), 124–130. https://doi.org/10.1016/J.MATCHEMPHYS.2012.11.029

Yin, B., Zhang, S., Jiang, H., Qu, F., & Wu, X. (2015). Phase-controlled synthesis of polymorphic MnO2 structures for electrochemical energy storage. *Journal of Materials Chemistry A*, *3*(10), 5722–5729. https://doi.org/10.1039/C4TA06943A

Young, M. J., Holder, A. M., George, S. M., & Musgrave, C. B. (2014). *Mechanism of Pseudocapacitive Charge Storage in MnO 2* (Vol. 00).

Yuan, Y., He, K., Byles, B. W., Liu, C., Amine, K., Lu, J., Pomerantseva, E., & Shahbazian-Yassar, R. (2019). Deciphering the Atomic Patterns Leading to MnO2 Polymorphism. *Chem*, *5*(7), 1793–1805. https://doi.org/10.1016/j.chempr.2019.03.021

Yuan, Y., Liu, C., Byles, B. W., Yao, W., Song, B., Cheng, M., Huang, Z., Amine, K., Pomerantseva, E., Shahbazian-Yassar, R., & Lu, J. (2019a). Ordering Heterogeneity of [MnO 6] Octahedra in Tunnel-Structured MnO 2 and Its Influence on Ion Storage. *Joule*, *3*(2), 471–484. https://doi.org/10.1016/j.joule.2018.10.026

Yuan, Y., Liu, C., Byles, B. W., Yao, W., Song, B., Cheng, M., Huang, Z., Amine, K., Pomerantseva, E., Shahbazian-Yassar, R., & Lu, J. (2019b). Ordering Heterogeneity of [MnO6] Octahedra in Tunnel-Structured MnO2 and Its Influence on Ion Storage. *Joule*, *3*(2), 471–484. https://doi.org/10.1016/J.JOULE.2018.10.026

Yuan, Y., Wood, S. M., He, K., Yao, W., Tompsett, D., Lu, J., Nie, A., Islam, M. S., & Shahbazian-Yassar, R. (2016). Atomistic Insights into the Oriented Attachment of Tunnel-Based Oxide Nanostructures. *ACS Nano*, *10*(1), 539–548. https://doi.org/10.1021/acsnano.5b05535

Zhou, F., Zheng, H., Zhao, X., Guo, Q., Ni, X., Shen, T., & Tang, C. (2005). Large-area synthesis of high-quality β-MnO2nanowires and the mechanism of formation through a facile mineralization process. *Nanotechnology*, *16*(10), 2072–2076. https://doi.org/10.1088/0957-4484/16/10/015